

## Shape-Based Approach for Full Field Displacement Calculation of Cellular Materials

Yi Xiao<sup>1</sup>, Qing H. Qin<sup>1</sup>

**Abstract:** In this paper, we propose a new approach of optical full-field measurement for displacement calculation on the surface of a cellular solid. Cell boundary points are sampled as nodes in the analysis. To find the nodal values of displacements the nodes are to be mapped onto their corresponding points in the deformed cell boundary by shape based point matching. A thin plate spline based robust point matching (TPS-RPM) approach is used instead of correlation of intensity pattern between two regions in traditional displacement measurement methods. The proposed approach involves multiple-step image processing including cell region segmentation, cell region matching and node matching. Consequently displacements at a given node can be found easily. Two numerical examples of cellular solids under compressive loading are considered for assessing the effectiveness and accuracy of the proposed algorithm. The results show that local displacements around cell boundaries on the surfaces of the specimen can be effectively determined with the shape based method, thus it appears that the proposed methods is promising for predicting displacements of complex cellular materials.

**Keywords:** cellular material; Shape-based approach; Delaunay triangulation

### 1 Introduction

Man-made cellular solids such as aluminum honeycombs, metallic or polymeric foams are an important class of engineering materials. They possess many unique physical and mechanical properties which make themselves as diverse materials used in practical engineering. One example is the cushioning function of cellular materials, being of low stiffness. Another example is the space-filling core materials used in sandwich panels, which are light in weight and high in strength for shear/compression [Gibson and Ashby (1999); Alkhader and Vural (2008)]. During the past decades, researchers have been endeavoured in understanding the relationships between the structures and properties of cellular solids in order to ef-

---

<sup>1</sup> Research School of Engineering, Australian National University, Canberra, ACT 2601, Australia.

fectively exploit these properties in engineering design. Mechanisms governing physical and mechanical properties of cellular solids with simple geometry, such as honeycombs, have been well identified by performing theoretical and experimental analyses [Gibson and Ashby (1999); Qin and Swain (2004)]. Structural parameters such as structure irregularity, cell shape, wall thickness and cell anisotropy were used to investigate yielding and collapse phenomena [Gibson and Ashby (1999); Dutcher and Marangoni (2005)] and crack initiation and propagation [Papka and Kyriakides (1994); Song et al. (2008)] of cellular solids. Despite these efforts, cellular solids are so far less understood and less documented than other classes of materials such as aluminium and glass [Dutcher and Marangoni (2005)]. New techniques for characterizing cellular solids with more general and complex structures are expected for generating wider range of man-made cellular solids and more diverse applications.

It is noticed that a number of methods for calculating optical full-field of displacement/strain and identifying effective material properties has been recently proposed for analysing performance of various engineering materials [Qin et al. (1998); Feng et al. (2003); Haddadi and Belhabib (2008)]. The optical full field measurement of displacement is usually conducted by finite element method [Qin and Mao (1996); Sun et al. (2005)] in which discrete nodes are selected and their exact values of displacement (nodal values) are found using various approaches of matching. Among these methods, the digital imaging correlation (DIC) has become increasingly popular in the past two decades due to its relatively simple principle and flexibility in its adjustable scales from micro to nanoscale [Kang et al. (2005); Zhang et al. (2006); Sousa et al. (2011)]. With the DIC method, the nodal displacements on the surface of a planar specimen are obtained by comparing correlatively a pair of digital images taken before and after the imposed deformation of the specimen [Kang et al. (2005)]. The idea of using the correlation of digital images as a displacement measurement tool appears to be introduced by Peters and Ranson [Peters and Ranson (1982)]. Since then, various subset-based DIC methods [Pan et al. (2009); Hua et al. (2011); Zhang et al. (2011)] have been developed, which can be viewed as the main streams in DIC technique. These methods find the displacement of a point (node) centered at a subset by searching the maximal correlation coefficient that is determined by examining the intensity pattern of the subset with the intensity pattern of subsets in the deformed image. The displacement field is obtained from the interpolation on the discrete node values using techniques such as least-squares polynomial fitting [Weisstein (1999)] and finite element smoothing [Sun et al. (2005)].

The major concern of the DIC technique is its accuracy [Vassoler and Fancello (2010)]. The subset size in subset-based methods may affects the accuracy of the

displacement estimation significantly [Lecompte et al. (2006)]. An inherent limitation of the subset-based DIC method is that the choice of the subset size must compromise between correlation accuracy, interpolation error and computational cost. For interpolation, the amount of interpolated pixels accounted to estimated the shape function in interpolation is affected by the subset size, and hence the accuracy can be affected. For correlation calculation, large subset size contains more information of intensity pattern but requires more computational time to perform cross correlation. Some problems of optimal subset size selection for a specimen with a continuous area have been addressed in a number of studies [Sun and Pang (2007); Pan et al. (2008); Triconnet et al. (2009)]. As for materials containing discontinuous areas such as pores, inclusions or cracks, the choice of subset size is even more difficult. Special treatments must be taken either to define the subset within the continuous region or to handle the discontinuity across the interface of two distinct areas (phases). These strategies have been applied to testing specimens with simple geometries containing a single hole [Lagattu et al. (2004); Hamilton et al. (2010)] or a single crack [Abanto-Bueno and Lambros (2002); Lopez-Crespo et al. (2009)].

To handle problems of a specimen with sparse distributed discontinuities in arbitrary shapes, improved subset-based DIC approaches with enhanced spatial resolution have been developed [Jin and Bruck (2005); Rethore et al. (2007); Chen et al. (2010); Poissant and Barthelat (2010); Sousa et al. (2011)]. Alternatively, the so-called extended digital image correlation (X-DIC) had been used by many researchers [Sun et al. (2005); Besnard et al. (2006); Rethore et al. (2008)] due to its excellent shape adaptability and smooth ability. The X-DIC discretizes an image area into finite elements (segments) which are linked by nodes. Unlike in the original subset based DIC methods where the displacements are found point by point, all the nodal values in the X-DIC approach are correlated simultaneously by various matching algorithms. Despite both approaches are suitable for specimens with sparse distributed discontinuities, the accuracy of the measured displacements near the boundary of a specimen may not be as good as that of the interior points [Sun et al. (2005)]. In addition, the computational cost of these approaches is much higher. A mixed approach is recently proposed by applying X-DIC around the holes and original DIC in the rest regions. It takes the advantage of the adaptability of X-DIC and the high accuracy/lower cost of the original DIC (Zhang et al., 2011). However, the performance of the approach still relies on the subset size and the texture pattern of pixel's intensity in the subset.

As mentioned above, current displacement field calculations such as the original DIC and X-DIC are pixel-based, where intensity patterns in images are compared via correlation metrics. For a cellular solid, its surface has dominant cell walls that

are relatively thin. The subset size in cell wall regions can only be set very small. It is inefficient to spatially characterize the intensity pattern in such a subset area, dampening the displacement field calculation performance using original subset-based or X-DIC methods.

In this study, we present a new shape-based method aiming at retrieving displacement results of cellular solids measured from various experiments. The displacement field on the surface is obtained from the interpolation on the known nodal values. In the process of nodal displacement calculation, a set of nodes from a reference cell and the corresponding node set of the deformed cell are matched by a TPS-RPM method, which was originally developed in computer vision and pattern recognition [Chui and Rangarajan (2003)] for image registration and shape matching. The proposed nodal value calculating involves a multiple-step image processing to locate cell boundaries from raster images and establish mapping between nodes before and after deformation.

The rest of this paper is organized as follows. Section 2 describes the procedure of displacement field calculation as well as details of the shape-based nodal value calculation. Section 3 presents and analyses the numerical results from the point matching algorithm and displacement field calculation. In the end, some conclusions are given in section 4.

## 2 Displacement field calculation

### 2.1 Procedure

The proposed approach for displacement field calculation involves a series of image processing techniques, including cell region segmentation, cell region matching and cell boundary point matching.

Image segmentation is used to locate cell regions and their boundaries in an image. The open space which has higher illumination values is separated from cell walls which have considerably lower illumination values via a thresholding process. During the process, individual pixels in the image are marked as "cell" pixels (with a value of "1") if their value is less than a threshold value and as "open space" pixels (with a value of "0") otherwise. The key to have the regions segmented exactly along the cell boundaries is the choice of the threshold value. In our analysis, trial-and-error is used to determine this threshold value.

A binary image containing many blobs (or regions) is created after the thresholding process. A blob is a cell region consisting of a set of connected 'cell' pixel with the value of "1". Specks (small blobs) may be generated during the process of binarizing and are removed by judging the pixel number in a blob.

Matching a reference cell region to its deformed cell region, in this study, is an issue of having a region in an image and finding its closet match among a set of regions in another image. A so-called maximum-overlapping-area criterion is proposed for processing cell region matching: let  $R_k$  be the region of cell  $k$  in the reference image and  $R'$  be the corresponding region of cell  $k$  in the deformed image.  $R'$  is identified by  $S(R_k, R') = \max\{S(R_k, R'_i) | i=1,2,\dots,n\}$ . Here  $S(R_k, R'_i)$  is the number of pixels in the intersecting area of the two regions  $R'_i$  and  $R_k$ , and  $n$  is the total number of cell regions in the deformed image. The criterion is based on the fact that cell regions in the image of the compressed specimen deform in shape but have small change in locations (i.e. the small displacement problem).

In the proposed approach, boundary points in a cell region are extracted as nodes. The nodes in a reference cell are matched to their corresponding nodes in the deformed cell by a TPS-RPM. The detail procedure of the TPS-RPM used for node matching is described in the next section. Nodal displacements (values) are calculated from the pairs of matched nodes. Displacements at any other points in the open space bound by cell boundaries are then found by the natural neighbour interpolation, which is based on the method of Delaunay triangulations [Xiao and Yan (2003)]. It is superior to other interpolation methods in obtaining a continuous surface when the distribution of the data is anisotropic or data density varies.

## 2.2 TPS-RPM for node matching

### 2.2.1 Background

Thin plate spline robust point matching (TPS-RPM) is a point matching process that establishes point correspondence between a set of points before and after deformation. It can turn into a process of searching for an optimal transformation as well as the correspondence between the two sets. In general, the solution of point matching is not straight forward since both the correspondence and transformation are unknown. Furthermore, many factors such as the noise, outliers, and high-order deformations may increase the complexity of point matching problem. Researchers normally process this problem iteratively: optimal solution of the correspondence is produced when the transformation is known, and vice versa.

Robust point matching (RPM) [Gold et al. (1995); Rangarajan et al. (1996)] is an algorithm that jointly finds correspondences and rigid transformation parameters between two point sets (i.e., reference and deformed sets). In RPM, correspondence is parameterized as a permutation. Given the value of spatial mapping parameters, the correspondence problem is fitted into a linear assignment problem [Bertsekas and Tsitsiklis (1989; Burkard et al. (2009))]. To find the optimum solution to the assignment problem, a deterministic annealing scheme [Rangarajan et

al. (1996); Rose (1998)], embedded with the soft-assign technique [Kosowsky and Yuille (1994); Rangarajan et al. (1996)] is adopted. The deterministic annealing aims to avoid many poor local optima and it is independent of initialization with appropriate temperature [Rose (1998)]. The basic idea of the soft-assign is used to turn fuzzy correspondence matrix into a binarization which indicates the one-to-one correspondence between two point sets. Given correspondence variables, the spatial mapping parameters can be found efficiently by the standard numerical methods such as the least-square approximation. With the combination of deterministic annealing and soft-assign techniques, the RPM algorithm iteratively solves the spatial mapping and finds the correspondent variables at each temperature setting in the deterministic annealing process.

The TPS-RPM algorithm [Chui and Rangarajan (2003)] extends the use of RPM to a non-rigid transformation by applying thin-plate spline (TPS) to parameterize transformation. It estimates the correspondence and non-rigid transformation between two point-sets with different sizes. The redundant points are rejected as outliers. The soft-assign operation performs outlier rejection in addition to assign the point correspondences.

### 2.2.2 Problem Formulation

Consider two point sets,  $\mathbf{X} = \{\mathbf{x}_i : i = 1, 2, \dots, N_1\}$  along the reference cell boundary and  $\mathbf{Y} = \{\mathbf{y}_j : j = 1, 2, \dots, N_2\}$  along the deformed cell's boundary, we apply TPS-RPM to determine the correspondence between  $\mathbf{X}$  and  $\mathbf{Y}$  and match them accordingly (Chui and Rangarajan, 2003; Yang, 2011). According to Chui and Yang's work, the following energy function can be minimized:

$$E(\mathbf{M}, f) = \sum_{j=1}^{N_2} \sum_{i=1}^{N_1} m_{ij} \|\mathbf{y}_j - f(\mathbf{x}_i)\|^2 + \lambda \|L_f\|^2 + T \sum_{j=1}^{N_2} \sum_{i=1}^{N_1} m_{ij} \log m_{ij} - \zeta \sum_{j=1}^{N_2} \sum_{i=1}^{N_1} m_{ij} \quad (1)$$

which subjects to the following constraints,

$$\left\{ \begin{array}{ll} 0 \leq m_{ij} \leq 1 & \text{for } i = 1, 2, \dots, N_1 + 1; \quad j = 1, 2, \dots, N_2 + 1 \\ \sum_{j=1}^{N_2+1} m_{ij} = 1 & \text{for } i = 1, 2, \dots, N_1 \\ \sum_{i=1}^{N_1+1} m_{ij} = 1 & \text{for } j = 1, 2, \dots, N_2 \end{array} \right. \quad (2)$$

where the matrix  $\mathbf{M}$  characterize the correspondence between  $\mathbf{X}$  and  $\mathbf{Y}$  as follows

$$\mathbf{M} = \begin{pmatrix} m_{11} & \cdots & m_{1,N_2} & m_{1,N_2+1} \\ \vdots & \ddots & \vdots & \vdots \\ m_{N_1,1} & \cdots & m_{N_1,N_2} & m_{N_1,N_2+1} \\ m_{N_1+1,1} & \cdots & m_{N_1+1,N_2} & 0 \end{pmatrix} \quad (3)$$

It consists of two parts. The  $N_1 \times N_2$  inner sub-matrix defines the correspondence between  $\mathbf{X}$  and  $\mathbf{Y}$ . If  $\mathbf{x}_i$  corresponds to  $\mathbf{y}_j$ , then  $m_{ij} = 1$ , otherwise  $m_{ij} = 0$ . The  $(N_2 + 1)$ <sub>th</sub> column and the  $(N_1 + 1)$ <sub>th</sub> row define the outliers in  $\mathbf{X}$  and  $\mathbf{Y}$ , respectively. If  $\mathbf{x}_i$  (or  $\mathbf{y}_j$ ) is an outlier, then  $m_{i,N_2+1} = 1$  (or  $m_{N_1+1,j} = 1$ ).

$f$  denotes the non-rigid spatial transform between  $\mathbf{X}$  and  $\mathbf{Y}$ , with the form of  $f(\mathbf{x}_i) = \mathbf{x}_i \cdot \mathbf{a} + \mathbf{k}(\mathbf{x}_i) \cdot \mathbf{w}$ , in which  $\mathbf{a}$  is a  $3 \times 3$  matrix representing the affine transform and  $\mathbf{w}$  is a  $N_1 \times 3$  matrix representing the non-affine warping transform.  $\mathbf{k}_j(\mathbf{x}_i)$  is a kernel for TPS. In this study,  $\mathbf{k}_j(\mathbf{x}_i) = \|\mathbf{x}_j - \mathbf{x}_i\|^2 \log \|\mathbf{x}_j - \mathbf{x}_i\|$ , for  $i = 1, 2, \dots, N_1; j = 1, 2, \dots, N_2 + 1$ .

Under the mapping  $f$ , the point set  $\mathbf{X}$  is transformed to  $\mathbf{X}' = \{\mathbf{x}'_i : i = 1, 2, \dots, N_1\}$ . The first term In Eq (1) is a linear assignment- least square energy measurement,  $L$  in the second term is an operator denoting the smoothness regularization of  $f$ , with

$$\|Lf\|^2 = \iint [(\frac{\partial^2 f}{\partial u^2})^2 + 2(\frac{\partial^2 f}{\partial u \partial v})^2 + (\frac{\partial^2 f}{\partial v^2})^2] dudv \quad (4)$$

where  $u$  and  $v$  represent the two coordinates of the points. The entropy term (the third term) in Eq (1) is to control the fuzziness of the energy function in the deterministic annealing process.  $T$  is called the temperature parameter, which decreases gradually during the process. The last term in Eq (1) is designed to prevent excessive outlier rejection.  $\lambda$  and  $\zeta$  are the weighting parameters to balance these terms.

The TPS-RPM algorithm adopts the soft-assign and deterministic annealing techniques to convert the binarized correspondence problem to a continuous one and thus achieves a robust point matching. This technique attempts to find the global optimum of the energy function at high temperature and tracks it as the temperature decreases. The entropy term enables the fuzzy correspondence matrix to improve gradually and continuously during the optimization process instead of jumping around in the space of binary permutation matrices and outliers.  $\mathbf{M}$  converges to binary and the outliers are identified naturally from  $\mathbf{M}$  while making  $T$  gradually approach zero

The TPS-RPM algorithm is featured with a two-step up-date process: update the correspondences by differentiating the energy function in Eq (1) with respect to

$\mathbf{M}$ , and setting the result to zero; update the transformation by the least-squares approach to solve for the TPS parameters. The update process is controlled by the annealing scheme. According to a linear annealing rate  $r$  ( $r < 1$ ), The temperature  $T$  is reduced with  $T_{t+1} = T_t \cdot r$ , starting from  $T_0 = T_{initial}$ . Repeat the two-step updates till the object function convergence at a final temperature  $T_{final}$ .

The details of the two-step update are as follows [Chui and Rangarajan (2003); Yang (2011)]

**Step 1:** Update the correspondence  $\mathbf{M}$  by fixing the transformation  $f$ . The correspondence for points ( $i = 1, 2, \dots, N_1$  and  $j = 1, 2, \dots, N_2$ ) is

$$m_{ij} = \frac{1}{T} \exp\left[\frac{\xi}{T} - \frac{(\mathbf{y}_j - f(\mathbf{x}_i))^T (\mathbf{y}_j - f(\mathbf{x}_i))}{T}\right], \quad (5)$$

the outliers possibilities in  $\mathbf{X}$  ( $i = 1, 2, \dots, N_1$ ) is

$$m_{i, N_2+1} = \frac{1}{T_0} \exp\left[-\frac{(\mathbf{y}_{N_2+1} - f(\mathbf{x}_i))^T (\mathbf{y}_{N_2+1} - f(\mathbf{x}_i))}{T_0}\right], \quad (6)$$

and the outliers possibilities in  $\mathbf{Y}$  ( $j = 1, 2, \dots, N_2$ ) is

$$m_{N_1+1, j} = \frac{1}{T_0} \exp\left[-\frac{(\mathbf{y}_j - \mathbf{x}_{N_1+1})^T (\mathbf{y}_j - \mathbf{x}_{N_1+1})}{T_0}\right] \quad (7)$$

where  $\mathbf{x}_{N_1+1}$  and  $\mathbf{y}_{N_2+1}$  are outlier cluster centres and  $T_0$  is the initial temperature value. Iterated row and column normalization algorithm is then applied to the resulted  $\mathbf{M}$  in Eqs (5)–(7) to satisfy the constraints in Eq (2),

$$m_{ij} = \begin{cases} \frac{m_{ij}}{\sum_{l=1}^{N_2+1} m_{il}} & i = 1, 2, \dots, N_1; j = 1, 2, \dots, N_2 + 1 \text{ (Row normalization)} \\ \frac{m_{ij}}{\sum_{l=1}^{N_1+1} m_{lj}} & i = 1, 2, \dots, N_1 + 1; j = 1, 2, \dots, N_2 \text{ (Column normalization)} \end{cases} \quad (8)$$

**Step 2:** Update the transformation  $f$  by fixing the correspondence  $\mathbf{M}$ . The TPS-RPM algorithm simplifies this step by minimizing the following standard TPS bending energy function, a simplified form of Eq (1):

$$E_{TPS}^0(f) = \sum_{i=1}^{N_1} \|\mathbf{z}_i - f(\mathbf{x}_i)\|^2 + \lambda \|Lf\|^2 \quad (9)$$

where

$$\mathbf{z}_i = \sum_{j=1}^{N_2} m_{ij} \mathbf{y}_j \quad (10)$$

and

$$\|Lf\|^2 = \text{trace}(\mathbf{w}^T \mathbf{K} \mathbf{w}) \quad (11)$$

with  $\mathbf{K}_{N_1 \times N_1}$  being the TPS kernel formed from the vector  $\mathbf{k}(\mathbf{x}_i)$ ,  $i = 1, 2, \dots, N_1$ . Let  $\mathbf{Z} = \{\mathbf{z}_i : i = 1, 2, \dots, N_1\}$ . The minimization of Eq (9) produces a unique solution for  $f$ . By applying **QR** decomposition [[http://en.wikipedia.org/wiki/QR\\_decomposition](http://en.wikipedia.org/wiki/QR_decomposition) (visited in March 2012)] to  $\mathbf{X}$ ,

$$\mathbf{X} = (\mathbf{Q}_1 \ \mathbf{Q}_2) \begin{pmatrix} \mathbf{R} \\ \mathbf{0} \end{pmatrix} \quad (12)$$

where  $\mathbf{Q}_1$  and  $\mathbf{Q}_2$  are  $N_1 \times 3$  and  $N_1 \times (N_1 - 3)$  matrices, respectively, and  $\mathbf{R}$  is a  $3 \times 3$  upper triangular matrix, the TPS-RPM algorithm produces the optimal solution  $[\hat{\mathbf{a}}^0, \hat{\mathbf{w}}^0]$  as

$$\hat{\mathbf{w}}^0 = \mathbf{Q}_2 (\mathbf{Q}_2^T \mathbf{K} \mathbf{Q}_2 + \lambda \mathbf{I}_{(N_1-3)})^{-1} \mathbf{Q}_2^T \mathbf{Z} \quad (13)$$

$$\hat{\mathbf{a}}^0 = \mathbf{R}^{-1} \mathbf{Q}_1^T (\mathbf{Z} - \mathbf{K} \hat{\mathbf{w}}^0) \quad (14)$$

where  $\mathbf{I}_{(N_1-3)}$  is an  $(N_1 - 3) \times (N_1 - 3)$  identity matrix.

### 3 Assessment and discussion

To test the feasibility and efficiency of the proposed algorithm, two examples of cellular structures (a honeycomb specimen and a metallic foam specimen) are considered. The test specimens experienced compressive tests in the plane of a photograph (in-plane). The in-plane displacements of these cellular structures are calculated using the proposed algorithm.

#### 3.1 Parameter setting and point matching performance

In the process of point matching, the choice of initial value of  $T_{initial}$  is critical. When  $T_{initial}$  is too large, the point matching algorithm may be time consuming. When  $T_{initial}$  is too small, the algorithm may fail to converge to an optimal solution. To guarantee the point matching reaches a global optimal solution and keeps low computational cost,  $T_{initial}$  is set up as 10000 in our analysis, which is a value related to the largest squared distance of all point pairs. The temperature  $T$  is gradually reduced at an annealing rate of  $r = 0.53$ , which is a value trading off the speed of annealing procedure and accuracy of the point matching.

Due to the presence of outliers and perturbations along the boundaries, it is not always desirable for the TPS-RPM algorithm to obtain binary one-to-one correspondence between two point sets with  $T$  approaching zero [Chui and Rangarajan

(2003)]. And when  $T$  is too small, the affine mapping may have the risk of flip. The annealing process stops at a minimum value of  $T(T_{final})$  to avoid the flip of mapping. At  $T_{final}$ , most elements of matrix  $\mathbf{M}$  are close, although not equal, to values 0 or 1. And taking the points with the most significant  $m_{ij}$  as matched points, the algorithm achieves satisfied point matching result.

Since the initial values of elements in  $\mathbf{M}$  do not affect the elements' final values within  $[T_{initial}, T_{final}]$ , we set all initial entries of  $\mathbf{M}$  as  $1/N_1$ , and the outlier row and column are equal to  $1/100N_1$ . The initial values of  $\mathbf{a}$  and  $\mathbf{w}$  are  $\mathbf{a} = \mathbf{I}$  and  $\mathbf{w} = 0$ , where  $\mathbf{I}$  is an identity matrix.  $\mathbf{M}$ ,  $\mathbf{a}$  and  $\mathbf{w}$  are updated iteratively as  $T$  decreased.

The accuracy of the proposed displacement calculation depends on the performance of the point matching. In our assessment, the TPS-RPM algorithm rapidly brings two cell boundaries closer in space and more similar in shape from the initial iterations of the deterministic annealing procedure.

This assessment shows that the setting of final temperature  $T_{final}$  is deformation dependent. For the pairs of cell point sets that have small deformation, good matching is achieved at final iteration, and the sequential ordering of points is preserved. For some pairs of cell boundaries that are significantly deformed, when  $T$  is too small, the affine transform flipped, causing some points in a cell boundary map to points far away from their corresponding points in its deformed cell boundary and the sequential ordering of points is broken. Under our setting ( $T_{final} = 500$ ), the algorithm achieves satisfied point matching result. Only a few mismatches are introduced at the points in highly folded curves, but sequential ordering of points is preserved.

### **3.2 Numerical results for the honeycomb specimen under compression**

#### **3.2.1 Specification of the specimens**

The images of aluminum (AI-5052-H39) honeycomb specimens subjected to a compression are obtained from the experiment reported in [Papka and Kyriakides (1994)]. The experiment conducted in [Papka and Kyriakides (1994)] was displacement-controlled in a standard, screw-type electromechanical testing machine. The test specimen has  $9 \times 6$  cells cut from a  $0.6 \times 0.6$  m sheet of 15.9 mm thick honeycomb. The cells have hexagonal structures as shown in Fig. 1(a). The nominal cell size (perpendicular distance between two opposite cell walls which is in parallel) was 8.26 mm and the average cell wall thickness was 0.145 mm. The aluminium specimen was an elastic-plastic honeycomb. In compression, it showed a linear-elastic regime followed by a plateau of roughly constant stress, leading into a final regime of steeply rising stress. Each regime was associated with a mechanism of deformation which can be identified by loading and photographing

the honeycombs. At the start of loading process, some cell walls were bended, exhibiting linear elasticity. When a critical stress was reached some cells began to collapse in a cell wall with a plastic yield point. We now calculate the displacement between the two frames from configuration 1 to configuration 2 as shown in Fig. 1. The two configurations (configurations 1 and 2) of the specimen corresponded to the equilibrium states with a stress of 1 and 10 psi respectively. The specimen through these configurations was in a linear elasticity state and the cells experienced different degree of shape deformation, but the topology of cell boundaries in the two frames kept unchanged.

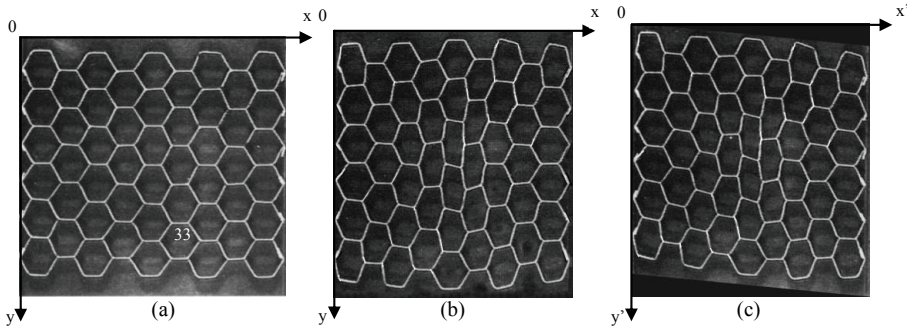


Figure 1: A honeycomb specimen subjected to a compression experiment. (a) Original image (Configuration 1 in [Papka and Kyriakides (1994)]); (b) Deformed image (Configuration 2 in [Papka and Kyriakides (1994)]); (c) Synthetic image transformed from the image shown in Fig 1 (b).

### 3.2.2 Point matching accuracy

Fig 2 (a) shows the point mapping between the 33<sub>th</sub> cell in Fig 1(a) and its corresponding cell in Fig 1 (b). The cell shape has a simple geometry and is in a shear deformation in y direction. There are 536 points along the reference cell boundary, extracted by the method described in Section 2.1. Most points are mapped to their correspondent points, only 12 points link to the neighbours of their correspondences.

For quantitative measurement of the accuracy of point matching, a simulated synthetic image (Fig 1 (c)) is generated. It is a shear transform ( $f_s : (x, y) \rightarrow (x', y')$ ) on the image shown in Fig 1(b).  $f_s$  here is the shearing parallel to the y axis, in the transformation form of

$$x' = x, \quad y' = y + kx. \quad (15)$$

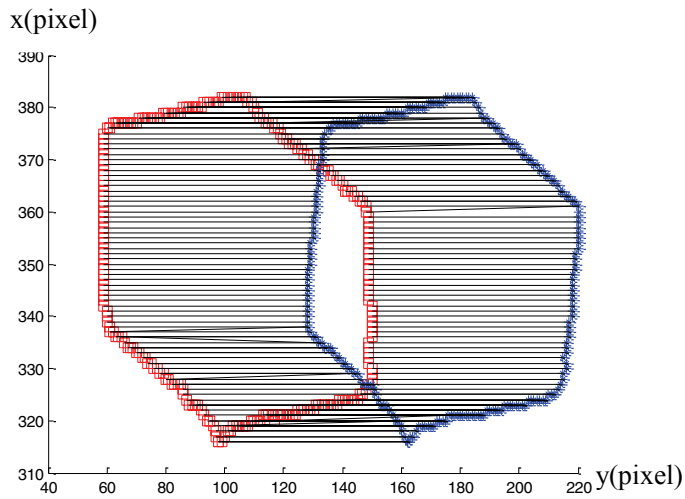


Figure 2: Point matching between a cell boundary and its deformed cell boundary (1 pixel = 0.09mm).

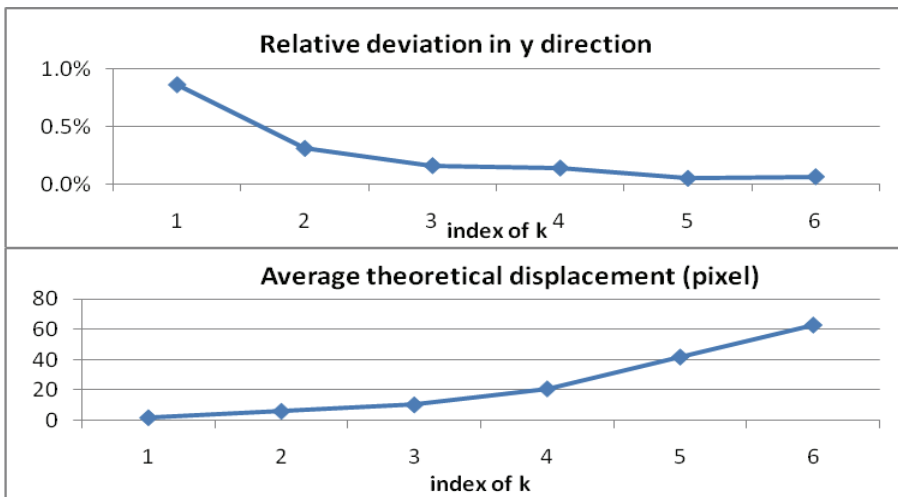


Figure 3: Average relative deviation and the theoretical displacement at different k for the ordered points of the cell shown in Fig 2 (1 pixel = 0.09mm).

For a given point  $P$ , the relative deviation between the mapped point of  $P$  obtained by TPS-RPM and the point of  $P$ 's shear transform is used for the point matching evaluation as follows:

$$D = \left| \frac{u_y - u'_y}{u_y} \right|, \quad (16)$$

where  $u_y$  is the displacement in  $y$  direction obtained from the shear transform shown in Eq. 15;  $u'_y$  is the displacement in  $y$  direction calculated by the proposed method. Fig 3 depicts the relative deviations of point pairs in  $y$  direction for the cell shown in Fig. 2, where the shear element  $k = \{0.01, 0.03, 0.05, 0.1, 0.2, 0.3\}$ , corresponding to the maximum displacements in  $y$  direction  $d_m(\text{pixel}) = \{4, 11, 19, 38, 76, 115\}$  respectively. All the average relative deviations are not larger than 0.01 in  $y$  direction. At  $k = 0.01$ , the average relative deviation is the largest one, being attributed to the digitalization and binarization of the image. Although the points are well matched, the bias of transformed cell boundary causes the deviations comparable to the displacements of the point pairs. When  $k$  increases, the number of mismatched point pairs only increases slightly. The increasing of deviation values is slower than the increasing of displacement, thus the relative deviation values decrease with the increase of  $k$ .

### 3.2.3 Displacement field analysis

The displacements of the honeycomb specimen from configurations 1 to 2 in  $x$  and  $y$  direction, calculated using our algorithm are shown in Fig 4. The reference point is at (0,0) in both images (Figs 1 (a) and (b)).  $x$  axis is in loading direction of the compression test. The gradient of displacement in  $x/y$  direction reflects the degree of deformation in that direction.

From Fig 4 we can see, the displacement in  $x$  direction increases with the increasing of  $y$ , and is symmetric about  $x$  axis but not  $y$  axis. The cells in the central columns are seen larger gradient of displacement than that of the cells toward the two end columns, thus these cells have larger deformations, while cells toward the two end columns and around the central row have smaller gradient of displacements and these cells remain almost unchanged in shape. It is interested to see that the cells that significantly deform in  $x$  direction form a hyperbola with its transverse axis in the horizontal central line  $y = 300(\text{pixel})$  and the center of the specimen as its center. The displacements of the cells in  $y$  direction are nonlinear with respect of  $y$ . The displacements are concentrated in the lower rows of the specimen and are symmetric about  $y$  axis but not  $x$  axis. The cells between the middle and bottom row of the fifth column suffer bigger deformations and the deformations spread to their

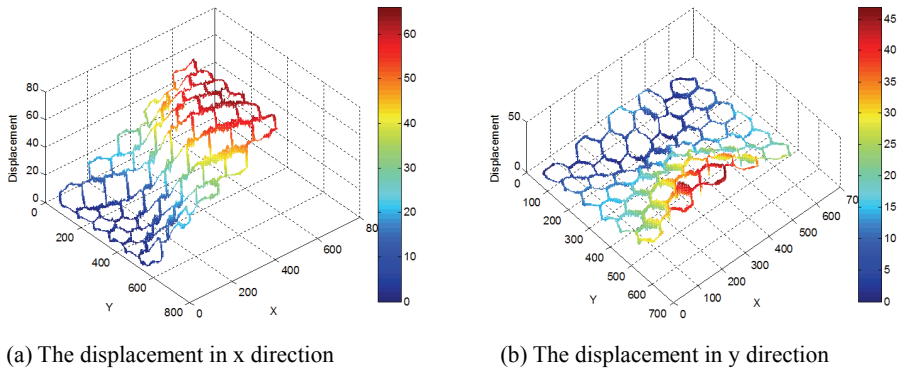


Figure 4: The displacement of the honeycomb specimen in x and y direction (1 pixel = 0.09mm).

neighbouring cells. The cells that are significantly deformed in y direction form an inverted V-shape in the lower portion of the specimen.

### 3.3 Numerical results for a designed specimen of metallic foams

#### 3.3.1 Specification of the metallic foam

The images of the designed dog-bone specimen of metallic foams under mesoscopic compression tests are obtained from [Song, He et al. (2008)]. In the specimen, the effective test zone (ETZ) was in dimensions 4mm×6mm×4.5mm. Upon loading, the stress level inside the ETZ was significantly higher than that of outside ETZ. The specimen has at least one complete cell located at the center of ETZ. It was sectioned by electro-discharge machining to avoid local damage to the cell walls. Uniaxial compression tests for the specimen were carried out in a small loading device, equipped inside a S570 SEM. Series images recording the cell morphology were acquired in the SEM at an interval of every 5% deformation. The tests were in the displacement-controlled mode with a crosshead speed of 2 mm/min, till 80% deformation was achieved.

We concern the images between the two frames from stage 0 and 1. Fig 5 (a) refers to the specimen within the ETZ in the initial stage (stage 0) with engineering strain  $\epsilon_E = 0$ . According to the description in [Song et al. (2008)], the local deformation related to the morphology and location of the cells. Cells at the edges of the specimen provided less mechanical support upon loading, and the stress level was relatively low. Stress concentrated mainly on the cell at the centre due to its location and the relatively thin cell walls. In stage 1 (with  $\epsilon_E = 10\%$ ) (Fig. 5 (b)),

compressive stress increased almost linearly with increasing strain till an apparent large strain, accompanied by the overall elastic deformation of the cell walls. Cell walls outside ETZ also experienced elastic deformation at this stage. The obvious defects in the cell wall 'A' induced further local stress concentration and weakened the wall strength. As a result, the first yield took place in cell wall 'A'.

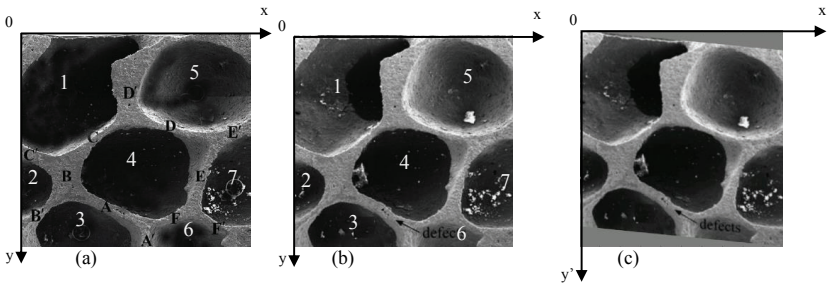


Figure 5: A specimen of metallic foam under a compression experiment (a) Original image (Stage 0); (b) Deformed image (Stage 1); (c) Synthetic image transformed from the image shown in Fig 5 (b).

### 3.3.2 Point matching accuracy

The point matching shown in Fig 6 is based on the 4<sup>th</sup> cell in Fig 5(a) and its corresponding cell in Fig 5 (b). The cell has complex geometry. There are 252 points along the reference cell boundary, extracted by the method described in Section 2.1. Most points in the cell boundary find their correspondences; a number of points mismatch to the points a few pixels away from their correspondences.

The evaluation method (it is the same as that in section 3.2.2) is carried out in this section. Fig 7 depicts the average relative deviations and theoretical displacement of point pairs in y direction for the cell shown in Fig 6, where the shear element  $k=\{0.01, 0.03,0.05,0.1,0.2,0.3\}$ , corresponding to the maximum displacements  $d_m(\text{pixel}) = \{3, 9,15,30,60,89\}$  respectively. All the average relative deviations are between 2%~5% in y direction. Unlike the honeycomb, the average relative diviation values for the matelic foam increase with the increase of  $k$  as the number of mismatched point pairs increases greatly with the increase of  $k$ ,causing the increasing of the average diviation value faster than the increasing of average displacement.

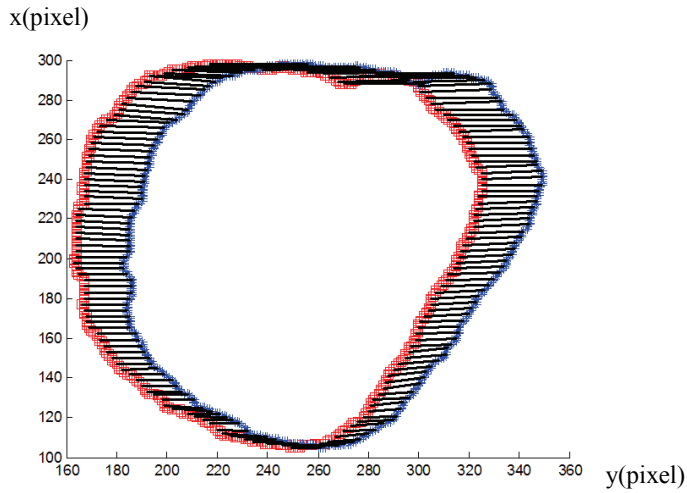


Figure 6: Point matching between the 4th cell boundary and its deformed cell boundary (1 pixel = 0.03mm).

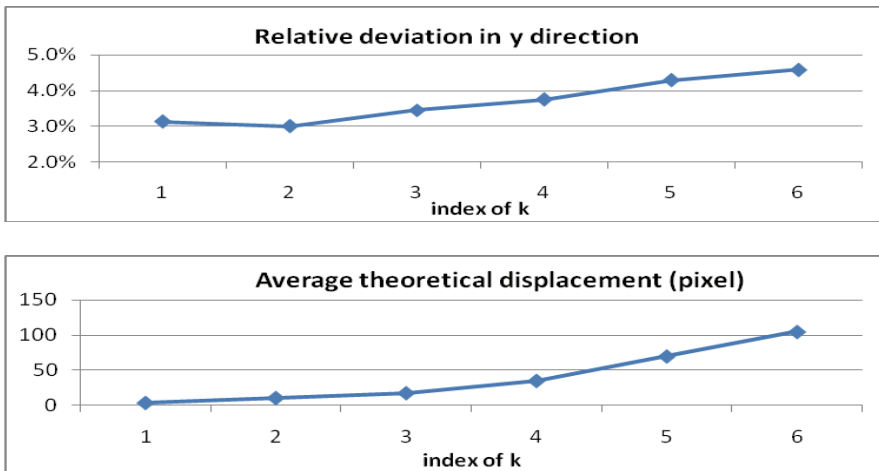


Figure 7: The average relative deviation and theoretical displacement of the ordered points at different for the cell shown in Fig 6 (1 pixel = 0.03mm).

### 3.3.3 Displacement field analysis

Figs 8(a) and (b) show the substrate displacement fields in  $x$  and  $y$  directions obtained by the proposed algorithm for the metallic foam from stage 0 to stage 1. The reference point is at  $(0,0)$  in both images (Figs 5(a) and (b)).

From the calculation we can see that the deformation is distributed irregularly in the metallic foam. The factors of location, orientation, thickness, and deflection can affect the deformation of a cell wall.

The displacement of cell walls in  $x$  direction is almost linearly changed with respect to  $y$  axis except cell walls 'C' and 'F' (see Figs 5 (a) and (b)) have larger gradient of displacement and cell walls 'A', 'D' and 'E' have smaller gradient of displacement. These indicate the smaller deformation of cell walls 'A', 'D' and 'E', and larger deformation on cell walls 'C' and 'F' in  $x$  direction.

In  $y$  direction, the overall displacement is much smaller ( $<0.15\text{mm}$ ) than that in  $x$  direction. There is a defect in cell wall 'A', which initiated a yield. Significant deformation occurs around the defect in cell 'A' in  $y$  direction. A hinge point is formed at the defect and cell wall 'A' is rotated as a hinge.

These results agree well with the visual observations and the simulation results mentioned in reference [Song, He et al. (2008)].

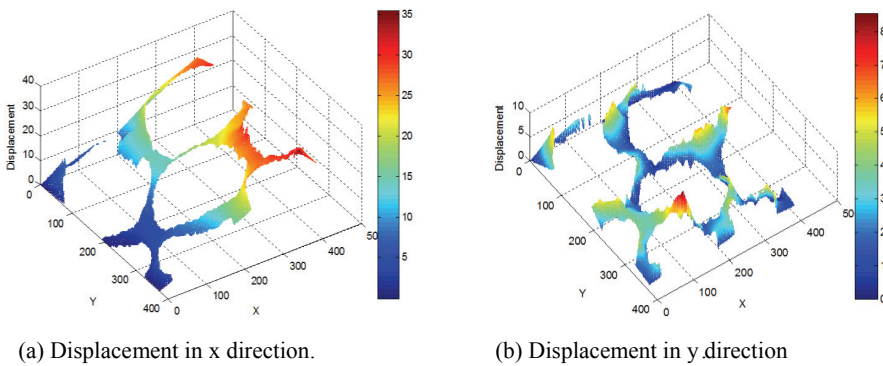


Figure 8: Displacement of the honeycomb specimen in  $x$  and  $y$  direction (1 pixel = 0.03mm).

## 4 Conclusion

The proposed method has two points different from the traditional DIC for full field displacement measurement. One is the node selection, the nodes are extracted from

the cell boundary; another is the method of node matching, the shape information of cells is used in this study for node matching.

The accuracy of the proposed method for displacement measurement is mainly determined by the performance of point matching, which is quantitatively measured by the relative deviation of displacement between the mapped points obtained by TPS-RPM and the true deformed points in a shear transform with different  $k$  from 0.01 to 0.3. The assessment shows that for a cell with simple geometry shape (honeycomb), the number of mismatched point pairs is small and this number increases slightly with the increase of  $k$ . The average relative deviation is less than 1%, and it is monotonically decreasing with respect to  $k$ ; for a cell with complex geometry shape (metallic foam), the number of mismatched point pairs is relatively larger (than that of honeycomb) and this number increases more significantly than that of honeycomb does, with the increase of  $k$ , when  $k > 0.01$ . The average relative deviation is between 2%~5% and it is monotonically increasing with respect to  $k$ , when  $k > 0.01$ . The results indicate that local displacements around holes' boundaries of a material's surface can be effectively determined with the proposed method under elastic deformation and it appears that the proposed method is promising for predicting displacements of complex cellular solids.

From the displacement fields of the honeycomb specimen and the metallic foam specimen calculated using the proposed algorithm, we found that maximum deformation occurs at the central area, and the location, orientation, thickness, and deflection affect the structure stability of materials. The results agree well with the visual investigations mentioned in reference [Song et al. (2008)], and with the simulation results of reference [Papka and Kyriakides (1994)]. The method provides the visualization of the local displacement of each cell, thus gives potential to systematic analysis of the mechanisms governing the quasi-static crushing of this class of materials.

## Reference

**Abanto-Bueno, J.; Lambros, J.** (2002): Investigation of crack growth in functionally graded materials using digital image correlation. *Engineering Fracture Mechanics*, vol. 69, no.14-16, pp. 1695-1711.

**Alkhader, M.; Vural, M.** (2008): Mechanical response of cellular solids: Role of cellular topology and microstructural irregularity. *International Journal of Engineering Science*, vol. 46, no.10, pp. 1035-1051.

**Bertsekas, D.P.; Tsitsiklis, J.N.** (1989): *Parallel and Distributed Computation: Numerical Methods*. Englewood Cliffs, NJ, Prentice-Hall.

**Besnard, G.; Hild, F.; Roux, S.** (2006): "Finite-Element" displacement fields anal-

ysis from digital images: Application to portevin-le chatelier bands. *Experimental Mechanics*, vol. 46, no.6, pp. 789-803.

**Burkard, R.E.; Dell'Amico, M.; Martello, S.** (2009): *Assignment Problems*. Philadelphia, SIAM (Society of Industrial and Applied Mathematics).

**Chen, J.; Zhang, X.; Zhan, N.; Hu, X.** (2010): Deformation measurement across crack using two-step extended digital image correlation method. *Optics and Lasers in Engineering*, vol. 48, no.11, pp. 1126-1131.

**Chui, H.L.; Rangarajan, A.** (2003): A new point matching algorithm for non-rigid registration. *Computer Vision and Image Understanding*, vol. 89, no.2-3, pp. 114-141.

**Dutcher, J.R.; Marangoni, A.G.** (2005): (ed.), *Soft Materials: Structure and Dynamics*. New York, CRC Press.

**Feng, X.Q.; Mai, Y.W.; Qin, Q.H.** (2003): A micromechanical model for interpenetrating multiphase composites. *Computational Materials Science*, vol. 28, no.3, pp. 486-493.

**Gibson, L.J.; Ashby, M.F.** (1999): *Cellular Solids: Structure and Properties*. Cambridge, Cambridge University Press.

**Gold, S.; Lu, C.P.; Rangarajan, A.; Pappu, S.; Mjolsness, E.** (1995): New algorithms for 2-D and 3-D point matching: pose estimation and correspondence. *Advances in Neural Information Processing Systems*. G. Tesauro, D. Touretzky and J. Alspector. Cambridge, MIT Press. 7:957-964.

**Haddadi, H.; Belhabib, S.** (2008): Use of rigid-body motion for the investigation and estimation of the measurement errors related to digital image correlation technique. *Optics and Lasers in Engineering*, vol. 46, no.2, pp. 185-196.

**Hamilton, A.R.; Sottos, N.R.; White, S.R.** (2010): Local strain concentrations in a microvascular network. *Experimental Mechanics*, vol. 50, no.2, pp. 255-263.

**Hua, T.; Xie, H.M.; Wang, S.M.; Hu, Z.X.; Chen, P.W.; Zhang, Q.M.** (2011): Evaluation of the quality of a speckle pattern in the digital image correlation method by mean subset fluctuation. *Optics and Laser Technology*, vol. 43, no.1, pp. 9-13.

**Jin, H.Q.; Bruck, H.A.** (2005): Theoretical development for pointwise digital image correlation. *Optical Engineering*, vol. 44, no.6, Article No. 067003.

**Kang, Y.L.; Zhang, Z.F.; Wang, H.W.; Qin, Q.H.** (2005): Experimental investigations of the effect of thickness on fracture toughness of metallic foils. *Materials Science and Engineering: A*, vol. 394, no.1, pp. 312-319.

**Kosowsky, J.J.; Yuille, A.L.** (1994): The invisible hand algorithm - solving the assignment problem with statistical physics. *Neural Networks*, vol. 7, no.3, pp. 477-490.

**Lagattu, F.; Brillaud, J.; Lafarie-Frenot, M.C.** (2004): High strain gradient measurements by using digital image correlation technique. *Materials Characterization*. vol. 53, no.1, pp. 17-28.

**Lecompte, D.; Smits, A.; Bossuyt, S.; Sol, H.; Vantomme, J.; Van Hemelrijck, D.; Habraken, A.M.** (2006): Quality assessment of speckle patterns for digital image correlation. *Optics and Lasers in Engineering*, vol. 44, no.10, pp. 1132-1145.

**Lopez-Crespo, P.; Burguete, R.L.; Patterson, E.A.; Shterenlikht, A.; Withers, P.J.; Yates, J.R.** (2009): Study of a crack at a fastener hole by digital image Correlation. *Experimental Mechanics*. vol. 49, no.4, pp. 551-559.

**Pan, B.; Asundi, A.; Xie, H.M.; Gao, J.X.** (2009): Digital image correlation using iterative least squares and pointwise least squares for displacement field and strain field measurements. *Optics and Lasers in Engineering*, vol. 47, no.7-8, pp. 865-874.

**Pan, B.; Xie, H.M.; Wang, Z.Y.; Qian, K.M.** (2008): Study on subset size selection in digital image correlation for speckle patterns. *Optics Express*, vol. 16, no.10, pp. 7037-7048.

**Papka, S.D.; Kyriakides, S.** (1994): In-plane compressive response and crushing of honeycomb. *Journal of the Mechanics and Physics of Solids*, vol. 42, no.10, pp. 1499-1532.

**Peters, W.H.; Ranson, W.F.** (1982): Digital imaging techniques in experimental stress-analysis. *Optical Engineering*, vol. 21, no.3, pp. 427-431.

**Poissant, J.; Barthelat, F.** (2010): A Novel "subset splitting" procedure for digital image correlation on discontinuous displacement fields. *Experimental Mechanics*, vol. 50, no.3, pp. 353-364.

**Qin, Q.H.; Mai, Y.W.; Yu, S.W.** (1998): Effective moduli for thermopiezoelectric materials with microcracks. *International Journal of Fracture*, vol. 91, no.4, pp. 359-371.

**Qin, Q.H.; Mao, C.X.** (1996): Coupled torsional-flexural vibration of shaft systems in mechanical engineering—I. Finite element model. *Computers & Structures*, vol. 58, no.4, pp. 835-843.

**Qin, Q.H.; Swain, M.V.** (2004): A micro-mechanics model of dentin mechanical properties. *Biomaterials*, vol. 25, no.20, pp. 5081-5090.

**Rangarajan, A.; Gold, S.; Mjolsness, E.** (1996): A novel optimizing network architecture with applications. *Neural Computation*, vol. 8, no.5, pp. 1041-1060.

**Rethore, J.; Hild, F.; Roux, S.** (2007): Shear-band capturing using a multiscale extended digital image correlation technique. *Computer Methods in Applied Me-*

*chanics and Engineering*, vol. 196, no.49-52, pp. 5016-5030.

**Rethore, J.; Hild, F.; Roux, S.** (2008): Extended digital image correlation with crack shape optimization. *International Journal for Numerical Methods in Engineering*, vol. 73, no.2, pp. 248-272.

**Rose, K.** (1998): Deterministic annealing for clustering, compression, classification, regression, and related optimization problems. *Proceedings of the IEEE*, vol. 86, no.11, pp. 2210-2239.

**Song, H.W.; He, Q.J.; Xie, J.J.; Tobota, A.** (2008): Fracture mechanisms and size effects of brittle metallic foams: In situ compression tests inside SEM. *Composites Science and Technology*, vol. 68, no.12, pp. 2441-2450.

**Sousa, A.M.R.; Xavier, J.; Morais, J.J.L.; Filipe, V.M.J.; Vaz, M.** (2011): Processing discontinuous displacement fields by a spatio-temporal derivative technique. *Optics and Lasers in Engineering*, vol. 49, no.12, pp. 1402-1412.

**Sun, Y.F.; Pang, J.H.L.** (2007): Study of optimal subset size in digital image correlation of speckle pattern images. *Optics and Lasers in Engineering*, vol. 45, no.9, pp. 967-974.

**Sun, Y.F.; Pang, J.H.L.; Wong, C.K.; Su, F.** (2005): Finite element formulation for a digital image correlation method. *Applied Optics*, vol. 44, no.34, pp. 7357-7363.

**Triconnet, K.; Derrien, K.; Hild, F.; Baptiste, D.** (2009): Parameter choice for optimized digital image correlation. *Optics and Lasers in Engineering*, vol. 47, no.6, pp. 728-737.

**Vassoler, J.M.; Fancello, E.A.** (2010): Error analysis of the digital Image correlation method. *Mecánica Computacional*, vol. XXIX, no.61, pp. 6149-6161.

**Weisstein, E.W.** (1999): Least Squares Fitting–Polynomial. From MathWorld - A Wolfram Web Resource:  
<http://mathworld.wolfram.com/LeastSquaresFittingPolynomial.html>.

**Xiao, Y.; Yan, H.** (2003): Text region extraction in a document image based on the Delaunay tessellation. *Pattern Recognition*, vol. 36, no.3, pp. 799-809.

**Yang, J.Z.** (2011): The thin plate spline robust point matching (TPS-RPM) algorithm: A revisit. *Pattern Recognition Letters*, vol. 32, no.7, pp. 910-918.

**Zhang, J.; Cai, Y.X.; Ye, W.J.; Yu, T.X.** (2011): On the use of the digital image correlation method for heterogeneous deformation measurement of porous solids. *Optics and Lasers in Engineering*, vol. 49, no.2, pp. 200-209.

**Zhang, Z.F.; Kang, Y.L.; Wang, H.W.; Qin, Q.H.; Qiu, Y.; Li, X.Q.** (2006): A novel coarse-fine search scheme for digital image correlation method. *Measurement*, vol. 39, no.8, pp. 710-718.

